

Highly Ordered Hierarchical Mesoporous MnCo₂O₄ with Cubic *Ia3d* Symmetry for Electrochemical Energy Storage

Changlong Xiao, Xinyi Zhang*, Tiago Mendes, Gregory P. Knowles, Alan Chaffee and Douglas R. MacFarlane*

School of Chemistry, Monash University, Victoria, 3800 Australia

***Corresponding author**

Tel: +61 3 9902 4618; +61 3 9905 4540:

E-mail address: xinyi.zhang@monash.edu; douglas.macfarlane@monash.edu

ABSTRACT. Highly ordered cubic $Ia3d$ mesoporous $MnCo_2O_4$ with crystalline framework was synthesized through a facile nanocasting method. The obtained mesoporous $MnCo_2O_4$ possesses hierarchical porosity with pore sizes of about 5 and 17 nm, respectively, and exhibits an enlarged surface area ($133\text{ m}^2/\text{g}$) compared to binary mesoporous Co_3O_4 ($98.6\text{ m}^2/\text{g}$) and MnO_2 ($75.0\text{ m}^2/\text{g}$). Significantly, the hierarchical mesoporous structure of $MnCo_2O_4$ is beneficial for exposing more electroactive sites, improving the charge transfer and facilitating the ion transport. As a consequence, the mesoporous $MnCo_2O_4$ shows a high charge storage performance of 199 mAh/g at current density of 1 A/g , long cycle stability and excellent rate capacity. This study demonstrates ordered ternary mesoporous materials with controllable porosity have great potential for high-energy-density electrochemical energy storage.

INTRODUCTION

The increasingly serious environmental problems associated with fossil fuels have prompted intense research interest into the development of sustainable and reliable energy storage systems. Among a wide variety of innovative technologies, supercapacitors (also known as electrochemical capacitors), as a type of rechargeable energy device, have attracted great attention owing to their high power density, minimal maintenance cost, long life span and fast charge/discharge ability compared to other conventional rechargeable technologies such as the lithium-ion battery.¹⁻⁶ The outstanding properties of supercapacitors make them important power source components for electric vehicles (including trams and buses), forklifts and other high power portable devices. The supercapacitor typically involves two identical electrodes that store charge in the double layer in the electrolyte adjacent to the electrodes. A variation on the supercapacitor is often described as a “hybrid supercapacitor” where one of the electrodes exhibits more battery-like behaviour and therefore improves the energy density of the device. There is much interest in such hybrid type devices made from inexpensive materials using very highly ion conductive KOH as the electrolyte, carbon as a classical double layer capacitive negative electrode and various transition metal oxide type materials as the positive electrode.⁷⁻¹¹ There have been many reports of these oxide type materials for this application, most describing these in terms of “pseudo-capacity”; however it has recently been pointed out^{12,13} that this description is incorrect in many cases (with the notable exception of MnO₂ and RuO₂) and that the main charge-discharge behaviour of these materials is Faradaic in nature. In other words, the bulk of the charge stored by these materials is electrochemical in nature and the process takes place over a narrow range of potentials, similar to battery electrodes. Nevertheless, as long as these materials are seen in the appropriate light, and analyzed as such, they remain interesting and important electrochemical materials for charge storage devices, in particular for hybrid type devices. As is true for all electrochemical storage

devices, it is the electrode capacity (in mAh g⁻¹) over the operating potential range that is the important feature of the electrode material. Therefore it is preferable to interpret the properties of hybrid materials in terms of specific capacity rather than specific capacitance (capacity = capacitance x ΔV).

Transition metal oxides and their hybrids are well-known electroactive materials owing to their multiple oxidation states. Recently, the development of earth abundant transition metal (Ni, Co and Mn etc.) oxide and hydroxide materials has attracted enormous research effort owing to their low environmental impact and theoretically high energy-density capability.¹⁴⁻¹⁹ Nonetheless, despite recent progress, great challenges still remain for non-noble electrode materials to achieve excellent capacity and stability performance. In pursuit of high electrochemically active surface area, exploration has been devoted to creating hierarchical and/or three-dimensional porous materials including metal oxides core/shell arrays,²⁰ NiCo₂O₄ nanosheet/halloysite nanotubes,²¹ porous graphene-like network films²² and mesoporous carbon and carbon nanotubes.²³ Among them, well-ordered mesoporous materials exhibit a unique set of advantages, including great numbers of regular channels, controllable structures and a multitude of composites.²⁴⁻²⁶ Lately, mesoporous first-row transition metal (e.g. Co, Ni and Fe) oxides have been reported as excellent electrochemical materials in energy conversion and storage, such as water splitting,²⁶⁻³⁰ however, most of them are unimodal mesoporous materials, with pore size less than 5 nm. Such small mesopores limit the access of the electrolyte and ion transport into the inner surface of the mesopores. Therefore, the surface area of the electrodes cannot be efficiently utilized, especially at high rates. In this regard, mesoporous materials with hierarchical porosity are of great current interest because they not only provide large active surface area, but also allow efficient mass transport.^{31,32}

As a typical spinel-type of ternary oxide, MnCo_2O_4 is known to have a cubic structure (space group $Fd-3m$ (227) with lattice constants of $a=b=c=8.269 \text{ \AA}$). It has wide applications in many fields, such as spintronics, sensors, lithium batteries, and electrochemical energy storage.³³⁻³⁷ MnCo_2O_4 nanostructures with different morphologies have been investigated.³⁵⁻⁴¹ However, there is no report on the synthesis of ordered hierarchical mesoporous MnCo_2O_4 as yet. In this work, we have synthesized cubic $Ia\bar{3}d$ mesoporous MnCo_2O_4 with crystalline framework. The resultant cubic $Ia\bar{3}d$ mesoporous MnCo_2O_4 has continuous crystalline framework with hierarchical pore sizes (ca. 5.4–17 nm) and high specific surface areas (up to $133 \text{ m}^2/\text{g}$). Such unique structure of the mesoporous MnCo_2O_4 allows efficient mass and charge transfer. Meanwhile, the combined contributions from both Co and Mn ions in MnCo_2O_4 make its performance superior to the binary counterparts, collectively exhibiting a high capacity, an excellent rate capability and long-term cycling performance.

EXPERIMENTAL SECTION

Chemicals. Cobalt (II) nitrate hexahydrate, manganese (II) nitrate tetrahydrate, potassium hydroxide, sodium hydroxide, Nafion 117 (5wt%), Pluronic P-123 ($\text{EO}_{20}\text{PO}_{70}\text{EO}_{20}$), tetraethyl orthosilicate (TEOS), urea and n-butanol were purchased from Sigma-Aldrich. All chemicals used in this study were analytical grade and used without further purification.

Preparation of mesoporous silica template (KIT-6). Cubic silica template (KIT-6) with ordered channels was synthesized through a hydrolysis approach followed by hydrothermal treatment. Typically, 6 g Pluronic P-123 was dissolved in acid solution containing 217 g distilled water and 11.8 g concentrated hydrochloric acid (35%) by vigorous stirring. Subsequently, 6 g n-butanol was added into the mixture solution with stirring at constant temperature (35 °C) using the oil bath until the formation of homogeneous solution, then 12.9 g TEOS was gradually added into the resultant solution. This resultant solution was sealed and vigorously stirred for another 24 hours at 35 °C for thorough hydrolysis of the silicone

precursor. Afterwards, the formed gel-like solution was transferred into an autoclave and placed in an oven for 24 hours at 100 °C. After the hydrothermal reaction, the sample was collected by filtration and dried in the oven. The dried sample was soaked in ethanol-HCl solution (20 mL ethanol/2 ml concentrated HCl) for another 20 min extraction treatment. Subsequently, the sample was washed with copious of water and dried again in an oven. Finally, the obtained powder was annealed in a tube furnace at 550 °C for 6 h to completely remove the residual polymer surfactant.

Preparation of mesoporous MnCo₂O₄. Mesoporous MnCo₂O₄ with well-ordered mesopores was synthesized through the hard-template method using the as-prepared KIT-6 template. Typically, 0.291 g Cobalt (II) nitrate hexahydrate and 0.125 g manganese (II) nitrate tetrahydrate with a molecular ratio of 2:1 were first dissolved in 10 mL absolute ethanol by vigorous stirring. Subsequently, 0.2 g as-prepared KIT-6 was added into the ethanol solution, followed by another 2 hour stirring to form a homogeneous suspension. After that, the resulting solution was heated and maintained at 60 °C using an oil bath to evaporate the ethanol. During the evaporation process, the metal ions will be forced to impregnate into the channels of the silica template. After the impregnation process, the obtained sample was annealed at 400 °C and 500 °C, respectively for another 2 hours. The final sample annealed at 400 °C was denoted as MnCo₂O₄ (400), while the sample annealed at 500 °C was denoted as MnCo₂O₄ (500), respectively. In order to fully fill the silica template, the impregnation and consolidation process was repeated with 1/3 of the metal precursor. Afterwards, the silica template was removed by washing with 2M NaOH solution three times and distilled water for another three times. Finally, mesoporous MnCo₂O₄ (400) and MnCo₂O₄ (500) was collected by centrifugation and dried in an oven at 60 °C overnight.

Preparation of MnCo₂O₄ nanoparticles. For comparison purposes, MnCo₂O₄ nanoparticles were prepared through a hydrothermal method. Specifically, Cobalt (II) nitrate hexahydrate (20 mM), manganese (II) nitrate tetrahydrate (40 mM) and urea (40 mM) were dissolved in a solution containing distilled water and absolute ethanol in a volume ratio of 4:1. Subsequently, the resulting solution was sonicated for 30 min before transferring to a 48 mL autoclave followed by hydrothermal treatment at 150 °C for 6 h. Afterwards, the sample was cooled to room temperature and washed with water several times to remove the residual impurities. Finally, the obtained MnCo₂O₄ nanoparticles were calcined at 400 °C for 2 h.

Electrochemical Measurements. The obtained mesoporous mMnCo₂O₄ (400) and a small amount of carbon black were drop-cast onto a nickel foam electrode (denoted as NF) to achieve the mMnCo₂O₄ (400) coated NF electrode (denoted as mMnCo₂O₄ (400)/NF). On the one hand, the mMnCo₂O₄ (400) is in direct contact with NF, thereby facilitating the electron transport. On the other hand, the macroscopic skeleton of Ni foam and the mMnCo₂O₄ (400) actually form two levels of hierarchical architecture, which can maximize the electrochemical surface area. Typically, 1 mg of the capacitive materials, 0.1 mg carbon black and 10 μL of Nafion solution were added to a 200 μL solution containing water and isopropanol with a volume ratio of 3:1. This suspension was sonicated until the formation of homogeneous black ink. After that, the ink was drop-cast onto a piece of nickel foam and dried making the material density 1mg/cm². The electrochemical performance in this study was evaluated in a three-electrode electrochemical cell employing the prepared MnCo₂O₄ (400)/NF as working electrode, Ag/AgCl (3 M KCl) and Pt wire as reference electrode and counter electrode, respectively. All measurements were conducted in 2 M KOH solution (pH = 14) on an EC-Lab electrochemical workstation. Electrochemical impedance spectra (EIS) were measured in a frequency range from 100 kHz to 0.01 kHz at an open circuit potential. The specific capacity was calculated based on the equation below:

$$C = Q/M = I\Delta t/3600M \quad (1)$$

where C (mAh g^{-1}) is the specific capacity, Q is the quantity of charge, I (mA) is the constant charge current, Δt (s) is the discharge time and M (g) represents the mass of the electroactive materials. For comparison purpose, mMnCo_2O_4 (500) and MnCo_2O_4 nanoparticle drop-casted nickel foam electrodes were also prepared through the drop-casting method described above. The following electrochemical measurements were identical to that outlined for the mMnCo_2O_4 (400)/NF electrode.

Material Characterization. The scanning electron microscopy images were conducted on field emission scanning electron microscope (Magellan 400 FEGSEM instrument). Transmission electron microscopic images and energy dispersive spectroscopy were recorded by a FEI Tecnai G2 T20 working at 200 kV. The X-ray diffraction patterns were obtained on a Bruker D8 ADVANCE ECO powder X-ray instrument using $\text{Cu K}\alpha$ radiation ($\lambda = 0.15418$ nm) in the 2θ range from 10° to 90° with a scanning step size of 0.01° . The small angle X-ray scattering experiment was conducted on N8 HORIZON small-Angle X-ray scattering system. The nitrogen adsorption-desorption isotherms were performed on a Tristar II instrument operating at 77 K. Prior to each measurement, the samples was degassed under vacuum environment for 5 hours at 150°C . The specific surface and pore size distribution was evaluated by Brunauer-Emmett-Teller (BET) method.

RESULTS AND DISCUSSION

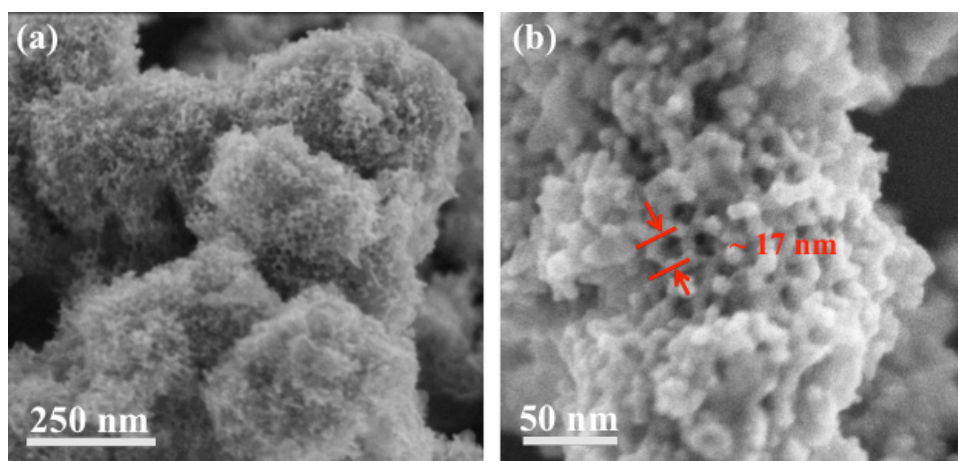


Figure 1. (a) SEM image and (b) high-resolution SEM image of hierarchically mesoporous MnCo_2O_4 .

Figure 1 presents the scanning electron microscopy (SEM) images of the obtained mesoporous MnCo_2O_4 calcinated at 400 °C (denoted as mMnCo_2O_4 (400)). As shown in **Figure 1a**, fluffy and interconnected nanoparticles with numerous nanocavities and nanopores are obtained via the nanocasting method. By a closer observation in **Figure 1b**, these fluffy nanoparticles are comprised of well-distributed mesopores with an average diameter around 17 nm. Significantly, these well-distributed mesopores are uniformly embedded among the entire bulk structure of each particle offering enormous open space and accessible channels. **Figure 2** displays the transmission electron microscopic (TEM) images of the synthesized mMnCo_2O_4 (400). It can be clearly observed that slit-like pores are well distributed among the entire mMnCo_2O_4 (400) nanoparticles with a bulk structure around 200 nm (**Figure 2a**). Two kinds of primary pores with average diameters of ~ 5 nm (**Figure 2a, 2b**) and ~ 17 nm (**Figure 2c, 2d**) can be observed, which is in agreement with previously reported Au and Fe induced mesoporous Co_3O_4 .^{28,42} All of these mesopores are well ordered showing a mesoporous structure with $Ia-3d$ symmetry, confirming the faithful replication of cubic structured KIT-6 template.

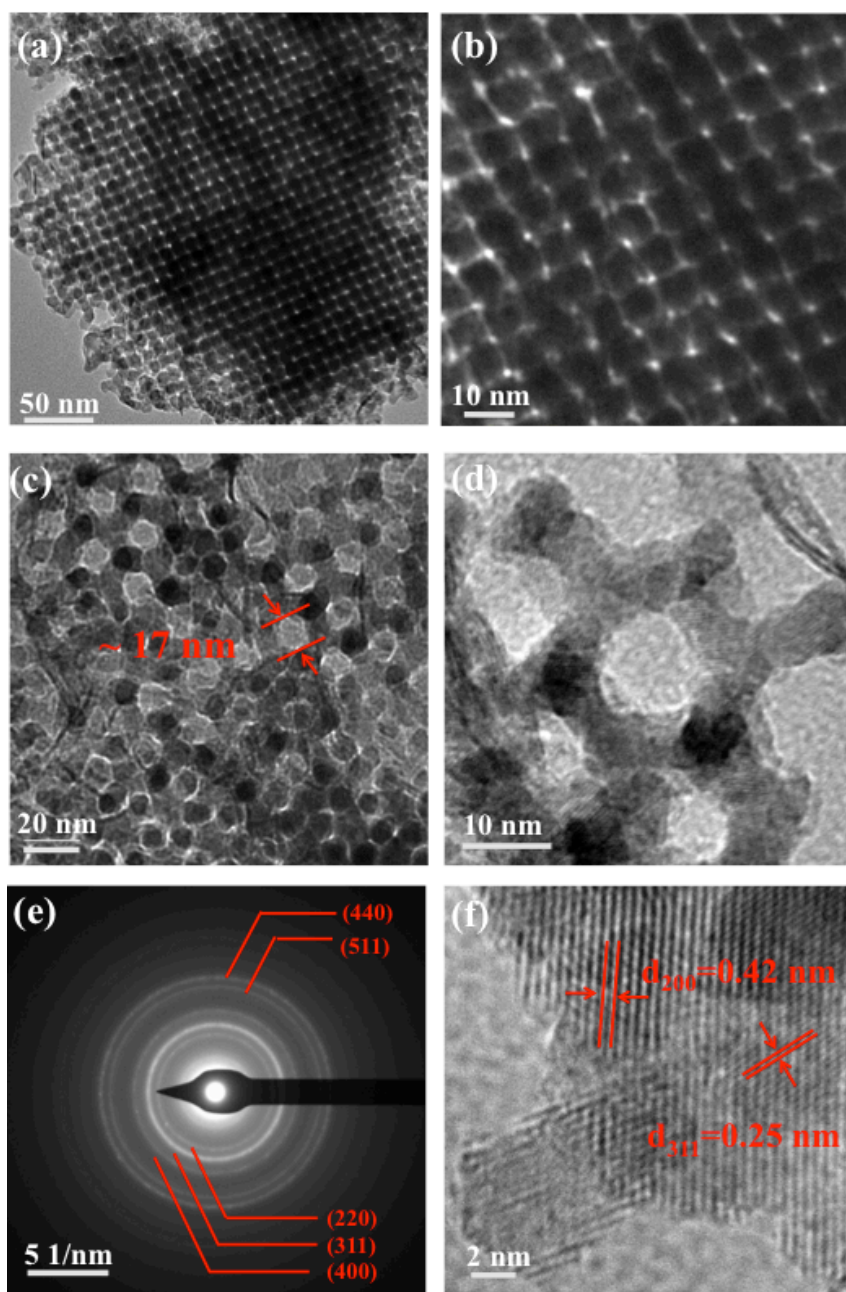


Figure 2. (a-d)TEM images at various magnifications , (e) SAED pattern and (f) high-resolution TEM image of well-ordered mMnCo₂O₄.

For comparison, mMnCo₂O₄ calcined at 500 °C, (denoted as mMnCo₂O₄ (500)) and MnCo₂O₄ nanoparticles (denoted as MnCo₂O₄ NPs) were also synthesized (see details in experimental section), as shown in **Figure S1**. Obviously, mMnCo₂O₄ (500) shows a similar porous structure to mMnCo₂O₄ (400), while MnCo₂O₄ NPs show irregular size from around 50 nm to 150 nm, and numerous irregular cavities are randomly distributed on the surface.

The mesoporous MnCo_2O_4 with well-ordered mesopores is expected to significantly enlarge the ion-accessible surface area which plays a crucial role in charge storage as the capacity performance is highly dependent on the Faradic redox reactions occurring on the interface between the electroactive materials and the electrolyte. Furthermore, high-resolution TEM (HRTEM) and selected area diffraction electron (SAED) patterns were also obtained to further investigate the surface structure of the obtained mMnCo_2O_4 . The HRTEM image of mMnCo_2O_4 (400), shown in **Figure 2f**, exhibits two kinds of lattice fringes with interplanar distance of 0.42 nm and 0.25 nm, which correspond to (200) and (311) atomic planes of cubic MnCo_2O_4 structure.⁴⁰ Meanwhile, the sharp diffraction fringes in the corresponding SAED pattern (**Figure 2e**) are corresponding to the (220), (311), (400), (440) and (511) crystal planes of the MnCo_2O_4 , indicating the high crystallinity of the mMnCo_2O_4 .³⁵

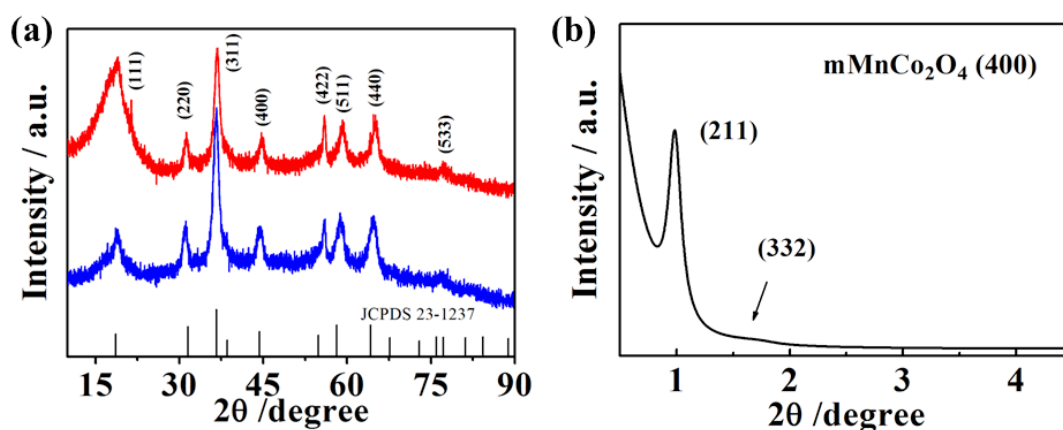


Figure 3. (a) Wide-angle X-ray diffraction patterns of mMnCo_2O_4 (400, red) and mMnCo_2O_4 (500, blue) and (b) Small-angle X-ray diffraction pattern of well-ordered mMnCo_2O_4 (400).

X-ray diffraction (XRD) measurement was further performed to characterize the crystalline structure of MnCo_2O_4 displayed in **Figure 3**. Both mMnCo_2O_4 samples (annealed at 400 °C and 500 °C) and MnCo_2O_4 NPs (**Figure S2**) show diffraction peaks at $2\theta = 18.6^\circ, 32.5^\circ, 37.2^\circ, 44.9^\circ, 56.3^\circ, 59.4^\circ, 65.1^\circ$ and 75.3° . All of these observed diffraction peaks can be indexed to the (111), (200), (311), (400), (422), (511), (440), and (533) planes of the cubic MnCo_2O_4 ($a=b=c=8.269 \text{ \AA}$; space group $Fd-3m$ (227), JPCDS card no. 23-1237). The

calculated average crystalline size is 11.6 nm by subtracting diffraction peak from instrument boarding. The low-angle XRD pattern in **Figure 3b** shows (211) and (332) diffraction peaks, which can further characterize the cubic ($Ia3d$) symmetry of the pore system. In addition, the small-angle X-ray scattering (SAXS) pattern in **Figure S2** shows that the $mMnCo_2O_4$ (400) has 3 well-resolved scattering peaks. After modelling analysis, it suggests that the $mMnCo_2O_4$ (400) contains mesopores with average diameter of 5.0 nm, which is consistent with the observation of slit-like pores (5.4 nm) in TEM image, indicating the highly ordered mesoporous architecture. The chemical composition and elemental distribution of the obtained $mMnCo_2O_4$ (400) were analyzed by energy dispersive X-ray spectroscopy (EDS) as shown in **Figure 4**. According to the backscattered TEM and elemental mapping images displayed in **Figure 4a-d**, both Mn and Co ions are uniformly distributed over the entire particle. In addition, an atomic Mn/Co ratio of approximately 1:2 was also determined by the EDS analysis shown in **Figure S3**, which is in accord with the empirical formula, further confirming the formation of cubic $Ia3d$ mesoporous $MnCo_2O_4$ spinel oxide structure.^{38,43}

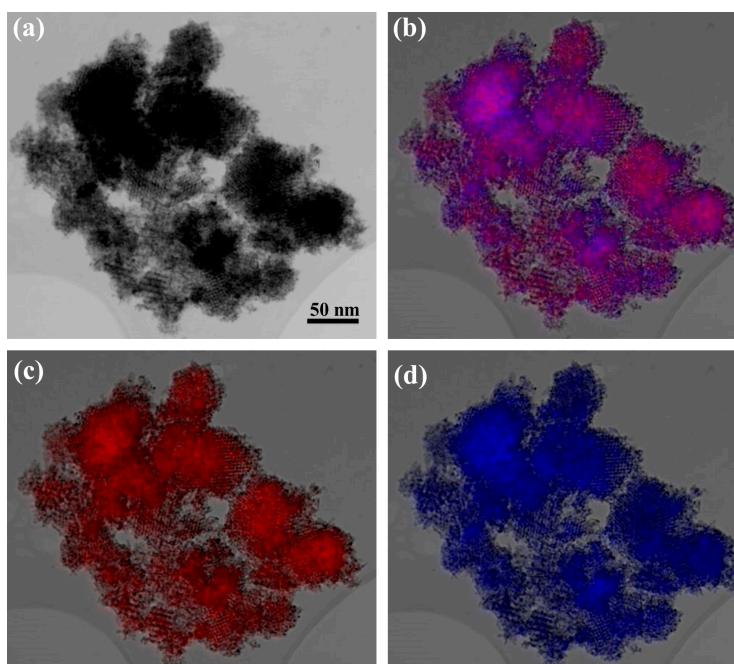


Figure 4. (a) Backscattered TEM image, (b-d) EDS Co (red) and Mn (blue) elemental mapping of $mMnCo_2O_4$.

Figure 5 presents the N₂ adsorption-desorption isotherms and pore size distributions of mMnCo₂O₄ (400), mMnCo₂O₄ (500) and MnCo₂O₄ NPs. The isotherms obtained from mMnCo₂O₄ (**Figure 5a**) exhibit the type IV features with H3 hysteresis loops, indicating the mesoporous nature of the mMnCo₂O₄.^{44,45} According to the calculated Brunauer-Emmett-Teller (BET) surface area data summarized in Table S1, both mMnCo₂O₄ (400) and mMnCo₂O₄ (500) have similar surface area with 133.3 m²/g and 132.8 m²/g, respectively, which are much higher than the value (45.2 m²/g) of MnCo₂O₄ NPs. Interestingly, mMnCo₂O₄ (400) has larger pore volume (0.420 cm³/g vs. 0.369 cm³/g) than mMnCo₂O₄ (500). The slight decrease in pore volume may result from the collapse of some large pores at higher annealing temperatures. This hypothesis is confirmed by the pore size distribution plots displayed in **Figure 5b**. The pore size distribution of mMnCo₂O₄ (400) exhibits two dominant peaks centered at 5.4 nm and 17.2 nm, while the dominant peaks of mMnCo₂O₄ (500) are located at 4.7 nm and 13.1 nm, respectively. All these results directly evidence the hierarchical characteristic of the mMnCo₂O₄ (400). It is expected that the high surface area and large pore volume of the hierarchical mesostructure can benefit the penetration of sterically hindered reactants into the internal layer, thereby dramatically enlarging the effective interfaces for electrochemical reactions.

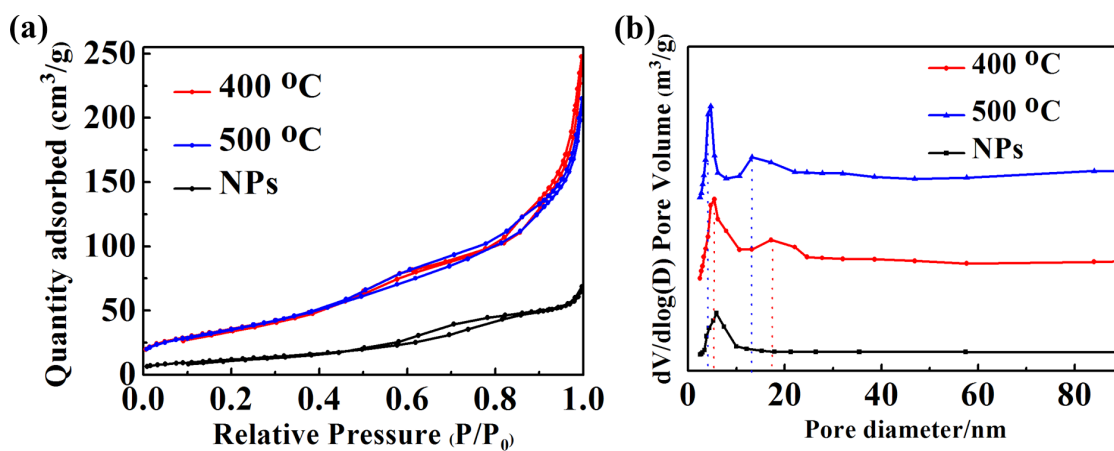


Figure 5. (a) N₂ adsorption desorption isotherms and (b) pore size distribution plots of mMnCo₂O₄ (400 °C), mMnCo₂O₄ (500 °C) and MnCo₂O₄ NPs.

Pristine mesoporous Co_3O_4 (mCo_3O_4) and MnO_2 (mMnO_2) were also prepared under the same conditions as mMnCo_2O_4 (400) for comparison. As shown in the TEM images (**Figure S4**), both mCo_3O_4 and mMnO_2 exhibit well-ordered mesoporous structures, revealing a successful replication of KIT-6. However, it can be seen in **Figure S5**, mCo_3O_4 exhibits only one dominant pore size centered at ~ 5 nm, while mMnCo_2O_4 shows two dominant peaks at ~ 5 nm and ~ 17 nm (**Figure 5**), respectively. According to the previous report, Co species can uniformly impregnate into both channels of KIT-6, forming a monomodal pore size distribution. However, the Co species are forced to impregnate into one channel in the presence of Fe ions, hence, the replica exhibits bimodal pore size distribution.^{27,28,42} In this study, the obtained mMnCo_2O_4 shows two kinds of pore size distributions, suggesting the Mn can also affect the impregnation of metal precursors inside the KIT-6. It has been reported that Mn ions would grow in only one set of the mesochannels, thus generating two kinds of mesopores after removing the KIT-6 (**Figure S5**).⁴⁶ However, it is difficult for pristine Mn ions to fully fill the mesochannel of KIT-6 owing to the complex interactions between the silica and the Mn alkali precursor.^{24,47} The outside loaded Mn may accumulate together to form a bulk structure, thereby decreasing the actual surface area (Table S1). Here, we propose that the Mn can guide the impregnation of the alkali precursors into the targeted KIT-6 mesochannels in the presence of Co precursor. As a result, the generated mMnCo_2O_4 shows excellent homogeneity and a hierarchically mesoporous structure. Significantly, the change in the porous structure leads to a higher surface area and pore volume of MnCo_2O_4 ($133 \text{ m}^2/\text{g}$, $0.42 \text{ cm}^3/\text{g}$) than that of the mCo_3O_4 ($98.6 \text{ m}^2/\text{g}$, $0.17 \text{ cm}^3/\text{g}$) and mMnO_2 ($75.0 \text{ m}^2/\text{g}$, $0.28 \text{ cm}^3/\text{g}$).

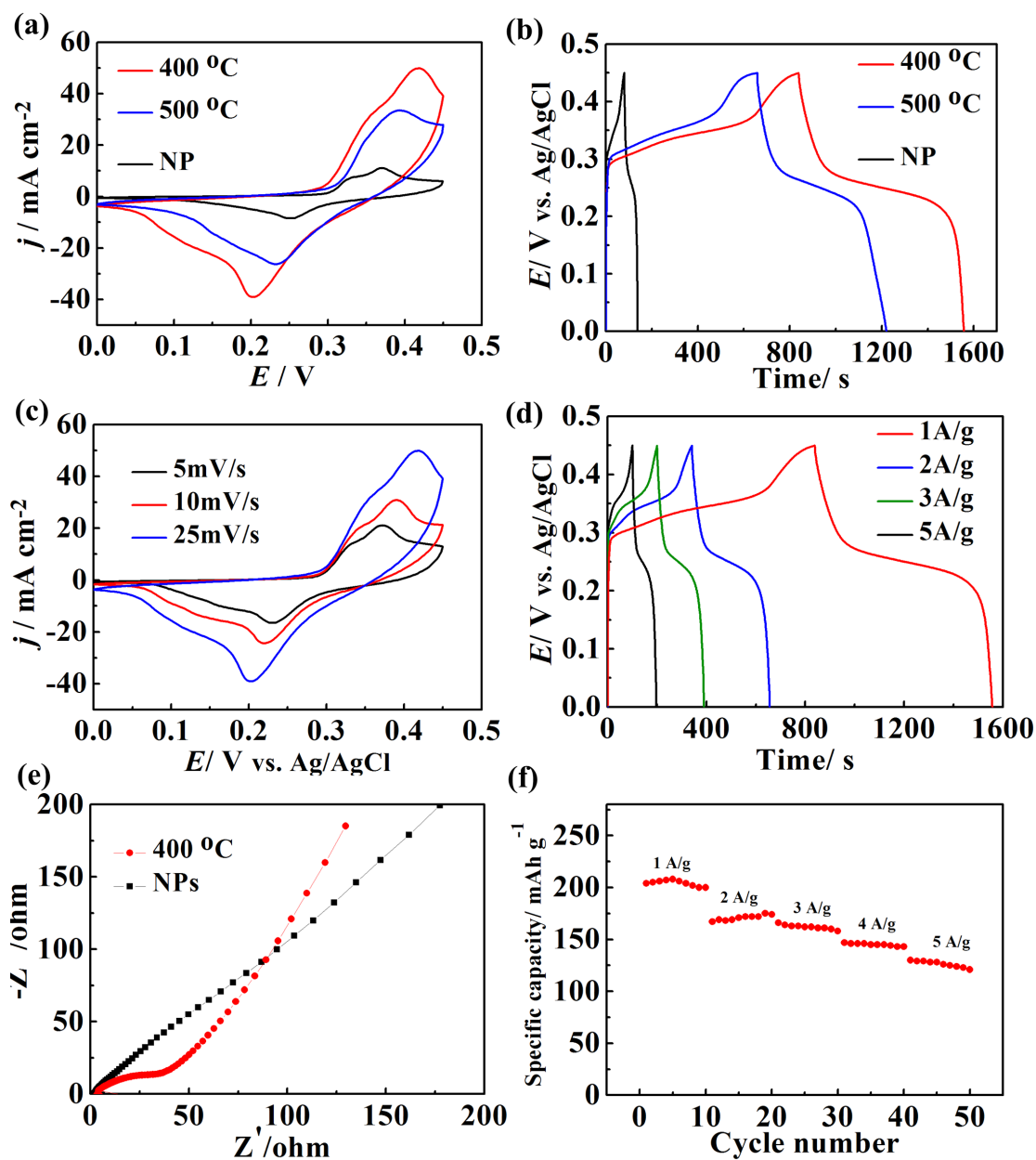


Figure 6. (a) CV curves of mMnCo_2O_4 (400), mMnCo_2O_4 (500) and MnCo_2O_4 NPs at a scan rate of 25 mV/s, (b) charge/discharge voltage profiles of mMnCo_2O_4 (400), mMnCo_2O_4 (500) and MnCo_2O_4 NPs at 1A/g, (c) CV curves of mMnCo_2O_4 (400) with various scan rates from 5 mV/s to 25 mV/s, (d) charge/discharge voltage profiles of mMnCo_2O_4 (400) at various current densities from 1 A/g to 5 A/g, (e) Nyquist plots of mMnCo_2O_4 (400) and MnCo_2O_4 NPs and (f) corresponding capacities of mMnCo_2O_4 (400) at different current densities.

The electrochemical performance of the obtained mMnCo_2O_4 samples and MnCo_2O_4 NPs were evaluated in 2 M KOH solution in a standard three-electrode electrochemical cell,

employing mMnCo₂O₄ loaded Ni foam working electrodes, a Ag/AgCl (saturated) reference electrode and a Pt wire counter electrode. **Figure 6a** depicts the cyclic voltammetry (CV) curves of all prepared MnCo₂O₄ samples at the scan rate of 25 mV/s in 2 M KOH solution. All CV curves exhibit similar shapes with two pairs of Faradaic redox peaks in the potential range from 0 V up to 0.45 V (vs. Ag/AgCl), corresponding to the chemical energy and electrical energy conversion as follows:⁴⁷⁻⁴⁹



Apparently, the CV curve obtained from mMnCo₂O₄ (400) has the largest enclosed area, suggesting the highest capacity.

To quantify their charge storage capability, galvanostatic charge-discharge (GCD) measurements were carried out within the potential window between 0 V to 0.45 V vs. Ag/AgCl (saturated) at a current density of 1A/g, as presented in **Figure 6b**. It can be observed that all MnCo₂O₄ samples exhibit plateau regions in their charge-discharge curves, as expected from the CV behavior. The specific capacities were calculated based on the discharge time of the GCD plots between 0.45 and 0.2 V according to Equation (1). The highest capacity is obtained from mMnCo₂O₄ (400) at the current density of 1 A/g (199 mAh g⁻¹), which is much higher than the values of mMnCo₂O₄ (500 °C, 155 mAh g⁻¹) and MnCo₂O₄ NPs (16.1 mAh g⁻¹). These results are consistent with the estimates obtained from the CV curves in **Figure 6a**. The theoretical capacity of MnCo₂O₄ compound was calculated to be 452 mAh g⁻¹ based on the redox potential (See calculation details in supporting information). The high specific capacity of mMnCo₂O₄ (400) outperforms many of recent reported non-precious electroactive materials in terms of charge storage capability, such as mesoporous Co₃O₄/CeO₂ hybrid nanowires (130 mAh g⁻¹),⁵⁰ Ni-Co-S composites (167 mAh

g^{-1})⁵¹ and flake-like MnCo_2O_4 (165 mAh g^{-1}),⁵² Urchin-like NiCo_2S_4 (175 mAh g^{-1})⁵³ and hierarchical Co_3O_4 twin-spheres (76 mAh g^{-1}),⁵⁴ as shown in Table S2.

Figure 6c shows the CV curves obtained from mMnCo_2O_4 (400) at various scan rates from 5 mV/s to 25 mV/s. Despite a slight shift in peak positions, the shapes of all CV curves basically remain unchanged, revealing a high electrochemical reversibility and excellent rate capacity. In addition, bare Ni foam was also characterized by CV and GCD techniques, shown in **Figure S6**. It can be observed that bare Ni foam shows a couple of redox peaks with low current densities (**Figure S6a**). This redox process is assigned to the reversible reaction of Ni(II)/Ni(III) occurred on the Ni foam surface. However, bare Ni foam exhibited negligible capacity compared with $\text{mMnCo}_2\text{O}_4/\text{NF}$ electrode shown in GCD curve (**Figure S6b**). **Figure S7a** depicts the initial and 5th cycle discharge curves of mMnCo_2O_4 (400)/NF electrode at current density of 5A/g. It reveals that the initial discharge capacity is around 125 mAh g^{-1} , while the capacity increases to 150 mAh g^{-1} after 5 cycles charge discharge process. This phenomenon is attributed to the gradual kinetic activation of mMnCo_2O_4 upon the ion transportation and redox process on the electrochemical interphase. Additionally, the CV profile (**Figure S7b**) also exhibits an activation process in the first 7 cycles (**Figure S7**), which is in agreement with the discharge data.

The GCD curves of mMnCo_2O_4 (400) obtained at various current densities from 1 A/g to 5 A/g are depicted in **Figure 6d**. It can be observed that specific capacity of 199 mAh g^{-1} , 172 mAh g^{-1} , 158 mAh g^{-1} , 145 mAh g^{-1} and 137 mAh g^{-1} can be obtained at current densities of 1A/g, 2 A/g, 3 A/g, 4 A/g and 5 A/g (**Figure 6f**), respectively. As a result, about 70% capacity is retained when the charge-discharge rate increases from 1 A/g to 5 A/g. These results are comparable, or, even better than those in the previous reports (Table S2).⁵⁰⁻⁵⁴ Moreover, the mMnCo_2O_4 (400) also exhibits higher capacity (199 mAh g^{-1}) than that of the corresponding monometallic oxides mCo_3O_4 (75 mAh g^{-1}) and mMnO_2 (56 mAh g^{-1}) (**Figure S8**),

suggesting the combined contribution from both Co and Mn ions produces enhanced charge storage capability. To check the materials loading effect, we further investigated the charge storage performance of mMnCo₂O₄ (400)/NF electrode with mass loading of 2 mg/cm². However, the capacity is lower than 1 mg/cm² materials loading (**Figure S9**). Higher mass loading may hinder the ion transport into the inner surface of mesoporous materials, and decrease the availability of internal surface of the electrode.

The mMnCo₂O₄ was further investigated by electrochemical impedance spectroscopy (EIS). The recorded Nyquist plots shown in **Figure 6e** were obtained after 50 cycles charge discharge measurement in fully charged state. The semicircle in the high frequency region is related to the charge transfer resistance within the capacitive materials (R_{ct}), and the straight slope in the low frequency reveal the ion diffusion on the electrode/electrolyte interface.^{21,54} It can be seen that the MnCo₂O₄ NP displays no obvious semicircle at high-frequency region, but a lowered slope at low-frequency region, suggesting its inferior ion diffusion process. In comparison, the mMnCo₂O₄ exhibits a smaller semicircle and a high slope, indicating a small internal resistance ($R_{ct} = 11.6 \Omega$), fast charge transfer and low ion diffusion resistance, which is even better than the reported flake-like MnCo₂O₄.⁵² The high capacity and good rate capability can be summarized as follow. Firstly, the mMnCo₂O₄ (400) with highly-ordered hierarchical mesopores and continuous crystalline framework can facilitate the transport of electrolyte ions, reducing the diffusion resistance, Secondly, the mesoporous MnCo₂O₄ has higher exposed surface area and offers more stable and efficient electroactive sites in comparison to its nanoparticle counterparts, resulting in the high capacitive performance. Thirdly, the porous structure of Ni foam allows rapid electron transfer and ion diffusion between MnCo₂O₄ and electrolyte on the entire electrode.

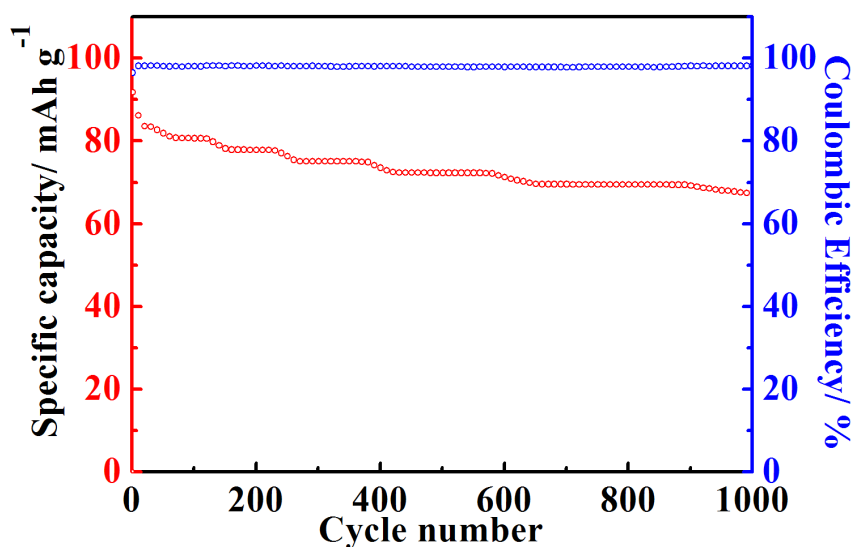


Figure 7. Cycling performance and coulombic efficiency of mMnCo₂O₄ (400)/NF electrode in 2 M KOH at a discharge current density of 10 A/g.

The stability and coulombic efficiency of the mMnCo₂O₄ (400) was tested with continuous charge-discharge cycling at a high current density of 10 A/g, as shown in **Figure 7**. In the first cycle, the mMnCo₂O₄ (400)/NF electrode can deliver a capacity of 93 mAh g⁻¹. After 1000 charge-discharge cycles, around 76% of the capacity is retained compared to the first cycle. Moreover, the coulombic efficiency at the first and last cycles is 96.5 % and 98.1 %, respectively, probably as a result of a small amount of oxygen production in the high potential region. As shown in **Figure S10**, the mesoporous structure is still maintained after 1000 cycles, suggesting the excellent stability of the mMnCo₂O₄. The slow decrease in the capacity with cycling process is mainly caused by the detachment of mMnCo₂O₄ from the Ni foam substrate. It is expected that the cycling stability can be further improved by using a more effective binder and optimized design of the electrode.

CONCLUSION

In summary, hierarchical mesoporous MnCo₂O₄ spinel oxide with two levels of hierarchy comprised by large mesopores (~17 nm) and small mesopores (~5 nm) has been synthesized.

A MnCo_2O_4 electrode has been developed by using Ni foam as the electron collector. The $\text{MnCo}_2\text{O}_4/\text{NF}$ hierarchical electrode material has high charge storage capability as well as excellent long-term cyclic stability, making it as a promising candidate for high-performance electrochemical energy storage devices. It is expected that this tunable, hierarchical mesoporous architecture can also be applied for other applications, such as batteries, fuel cells and water splitting devices.

SUPPORTING INFORMATION. The supporting information is available free of charge on the ACS publications website at DOI: XXXXXXXXXX.

TEM images of mMnCo_2O_4 (500) and MnCo_2O_4 NPs (Fig. S1), XRD diffraction pattern (Fig. S2), EDS spectrum (Fig. S3), TEM images of mCo_3O_4 and mMnO_2 (Fig. S4), N_2 adsorption/desorption isotherms (Fig. S5), electrochemical characterization of bare Ni foam (Fig. S6), mCo_3O_4 and mMnO_2 (Fig. S7), TEM of mMnCo_2O_4 (400) after cycling test (Fig. S8).

ACKNOWLEDGEMENT

The authors are grateful to the Australian Research Council for support under the Discovery Projects (DP: 120104334) and the Australian Laureate Fellowship programs. The authors acknowledge the use of facilities at the Monash Centre for Electron Microscopy.

REFERENCES

- (1) Miller, J. R.; Simon, P. Electrochemical capacitors for energy management. *Science* **2008**, *321*, 651-652.
- (2) Han, J.; Xu, G.; Dou, H.; MacFarlane, D. R. Porous Nitrogen-Doped Carbon Microspheres Derived from Microporous Polymeric Organic Frameworks for High Performance Electric Double-Layer Capacitors. *Chem. Eur. J.* **2015**, *21*, 2310-2314.

- (3) Chmiola, J.; Largeot, C.; aberna, P. L.; Simon, P.; Gogotsi, Y. Monolithic carbide-derived carbon films for micro-supercapacitors. *Science* **2010**, *328*, 480-483.
- (4) El-Kady, M. F.; Strong, V.; Dubin, S.; Kaner, R. B. Laser scribing of high-performance and flexible graphene-based electrochemical capacitors. *Science* **2012**, *335*, 1326-1330.
- (5) Simon, P.; Gogotsi, Y. Materials for electrochemical capacitors. *Nat. Mater.* **2008**, *7*, 845-854.
- (6) MacFarlane, D. R.; Forsyth, M.; Howlett, P. C.; Kar, M.; Passerini, S.; Pringle, J. M.; Ohno, H.; Watanabe, M.; Yan, F.; Zheng, W.; Zhang, S. Ionic liquids and their solid-state analogues as materials for energy generation and storage. *Nat. Rev. Mater.* **2016**, *1*, 15005.
- (7) Kurra, N.; Alhebshi, N. A.; Alshareef, H. N. Microfabricated pseudocapacitors using Ni(OH)₂ electrodes exhibit remarkable volumetric capacitance and energy density. *Adv. Energy Mater.* **2016**, *5*, 1401303.
- (8) Li, R.; Wang, Y.; Zhou, C.; Wang, C.; Ba, X.; Li, Y.; Huang, X; Liu, J. Carbon-Stabilized High-Capacity Ferroferric Oxide Nanorod Array for Flexible Solid-State Alkaline Battery–Supercapacitor Hybrid Device with High Environmental Suitability. *Adv. Funct. Mater.* **2015**, *25*, 5384-5394.
- (9) Dong, S.; Shen, L.; Li, H.; Pang, G.; Dou, H; Zhang, X. Flexible Sodium-Ion Pseudocapacitors Based on 3D Na₂Ti₃O₇ Nanosheet Arrays/Carbon Textiles Anodes. *Adv. Funct. Mater.* **2016**, *26*, 3703-3710.
- (10) Li, W.; Xin, L.; Xu, X.; Liu, Q.; Zhang, M.; Ding, S.; Zhao, M.; Lou, X. Facile synthesis of three-dimensional structured carbon fiber-NiCo₂O₄-Ni(OH)₂ high-performance electrode for pseudocapacitors. *Sci. Rep.* **2015**, *5*, 9277.
- (11) Zhao, Y.; Hu, L.; Zhao, S.; Wu, L. Preparation of MnCo₂O₄@Ni(OH)₂ Core–Shell Flowers for Asymmetric Supercapacitor Materials with Ultrahigh Specific Capacitance. *Adv. Funct. Mater.* **2016**, *26*, 4085-4093.

- (12) Brousse, T; Bélanger, D; Long, J. W. To be or not to be pseudocapacitive? *J. Electrochem. Soc.* **2015**, *162*, A5185-A5189.
- (13) Stoller, M. D.; Ruoff, R.S. Best practice methods for determining an electrode material's performance for ultracapacitors. *Energy Environ. Sci.* **2010**, *3*, 1294-1301.
- (14) Li, H. B.; Yu, M. H.; Wang, F. X.; Liu, P.; Liang, Y.; Xiao, J.; Wang, C. X.; Tong, Y. X.; Yang, G. W. Amorphous nickel hydroxide nanospheres with ultrahigh capacitance and energy density as electrochemical pseudocapacitor materials. *Nat. Commun.* **2013**, *4*, 1894.
- (15) Xia, X.; Tu, J.; Mai, Y.; Chen, R.; Wang, X.; Gu, C.; Zhao, X. Graphene sheet/porous NiO hybrid film for supercapacitor applications. *Chem. Eur. J.* **2011**, *17*, 10898-10905.
- (16) Gao, Z.; Yang, W.; Wang, J.; Song, N.; Li, X. Flexible all-solid-state hierarchical NiCo₂O₄/porous graphene paper asymmetric supercapacitors with an exceptional combination of electrochemical properties. *Nano Energy*, **2015**, *13*, 306-317.
- (17) Guo, D.; Luo, Y.; Yu, X.; Li, Q.; Wang, T.; High performance NiMoO₄ nanowires supported on carbon cloth as advanced electrodes for symmetric supercapacitors. *Nano Energy*, **2014**, *8*, 174-182.
- (18) An, C.; Wang, Y.; Huang, Y.; Xu, Y.; Jiao, L.; Yuan, H. Porous NiCo₂O₄ nanostructures for high performance supercapacitors via a microemulsion technique. *Nano Energy*, **2014**, *10*, 125-134.
- (19) Hong, W. T.; Welsch, R. E.; Shao-Horn, Y. Descriptors of oxygen-evolution activity for oxides: A statistical evaluation. *J. Phy. Chem. C* **2016**, *120*, 78-86.
- (20) Xia, X.; Tu, J.; Zhang, Y.; Wang, X.; Gu, C.; Zhao, X. B.; Fan, H. J. High-quality metal oxide core/shell nanowire arrays on conductive substrates for electrochemical energy storage. *ACS Nano* **2012**, *6*, 5531-5538.

- (21) Liang, J.; Fan, Z.; Chen, S.; Ding, S.; Yang, G. Hierarchical NiCo₂O₄ nanosheets@halloysite nanotubes with ultrahigh capacitance and long cycle stability as electrochemical pseudocapacitor materials. *Chem. Mater.* **2014**, *26*, 4354-4360.
- (22) Zhang, L. L.; Zhao, X.; Stoller, M. D.; Zhu, Y.; Ji, H.; Murali, S.; Wu, Y.; Perales, S.; Clevenger, B.; Ruoff, R. S. Highly conductive and porous activated reduced graphene oxide films for high-power supercapacitors. *Nano Lett.* **2012**, *12*, 1806-1812.
- (23) Frackowiak, E.; Metenier, K.; Bertagna, V.; Beguin, F. Supercapacitor electrodes from multiwalled carbon nanotubes. *Appl. Phys. Lett.* **2000**, *77*, 2421-2423.
- (24) Ren, Y.; Ma, Z.; Bruce, P. G. Ordered Mesoporous Metal Oxides: Synthesis and Applications. *Chem. Soc. Rev.* **2012**, *41*, 4909-4927.
- (25) Lu, X.; Ng, Y. H.; Zhao, C.; Gold nanoparticles embedded within mesoporous cobalt oxide enhance electrochemical oxygen evolution. *ChemSusChem*, **2014**, *7*, 82-86.
- (26) Xiao, C.; Lu, X.; Zhao, C. Unusual synergistic effects upon incorporation of Fe and/or Ni into mesoporous Co₃O₄ for enhanced oxygen evolution. *Chem. Commun.* **2014**, *50*, 10122-10125.
- (27) Tüysüz, H.; Hwang, Y. J.; Khan, S. B.; Asiri, A. M.; Yang, P. Mesoporous Co₃O₄ as an electrocatalyst for water oxidation. *Nano Research*, **2013**, *6*, 47-54.
- (28) Grewe, T.; Deng, X.; Tüysüz, H. Influence of Fe Doping on structure and water oxidation activity of nanocast Co₃O₄. *Chem. Mater.* **2014**, *26*, 3162-3168.
- (29) Liu, S.; Hu, L.; Xu, X.; Al-Ghamdi, A. A.; Fang, X. Nickel Cobaltite Nanostructures for Photoelectric and Catalytic Applications. *Small* **2015**, *11*, 4267-4283.
- (30) Sun, S.; Zhao, X.; Yang, M.; Wu, L.; Wen, Z.; Shen, X. Hierarchically ordered mesoporous Co₃O₄ materials for high performance Li-ion batteries. *Sci. Rep.* **2016**, *6*, 19564.

- (31) Yuan, C.; Yang, L.; Hou, L.; Shen, L.; Zhang, X.; Lou, X. W. D. Growth of ultrathin mesoporous Co_3O_4 nanosheet arrays on Ni foam for high-performance electrochemical capacitors. *Energy Environ. Sci.* **2012**, *5*, 7883-7887.
- (32) Yuan, C.; Li, J.; Hou, L.; Yang, L.; Shen, L.; Zhang, X. Facile template-free synthesis of ultralayered mesoporous nickel cobaltite nanowires towards high-performance electrochemical capacitors. *J. Mater. Chem.* **2012**, *22*, 16084-16090.
- (33) Meena, P. L.; Pal, S.; Sreenivas, K.; Kumar, R. Structural and Magnetic Properties of MnCo_2O_4 Spinel Multiferroic. *Adv. Sci. Lett.* **2015**, *21*, 2760-2763.
- (34) Zhang, Y.; Luo, L.; Zhang, Z.; Ding, Y.; Liu, S.; Deng, D.; Zhao, H.; Chen, Y. Synthesis of MnCo_2O_4 nanofibers by electrospinning and calcination: application for a highly sensitive non-enzymatic glucose sensor. *J. Mater. Chem. B*, **2014**, *2*, 529-535.
- (35) Ma, T. Y.; Zheng, Y.; Dai, S.; Jaroniec, M.; Qiao, S. Z.; Mesoporous MnCo_2O_4 with abundant oxygen vacancy defects as high-performance oxygen reduction catalysts. *J. Mater. Chem. A* **2014**, *2*, 8676-8682.
- (36) Fu, C.; Li, G.; Luo, D.; Huang, X.; Zheng, J.; Li, L. One-step calcination-free synthesis of multicomponent spinel assembled microspheres for high-performance anodes of Li-ion batteries: a case study of MnCo_2O_4 . *ACS Appl. Mater. Interfaces* **2014**, *6*, 2439-2449.
- (37) Li, L.; Zhang, Y. Q.; Liu, X. Y.; Shi, S. J.; Zhao, X. Y.; Zhang, H.; Ge, X.; Cai, G. F.; Gu, C. D.; Wang, X. L.; Tu, J. P.; One-dimension MnCo_2O_4 nanowire arrays for electrochemical energy storage. *Electrochim. Acta*, **2014**, *16*, 467-474.
- (38) Cao, X.; Wu, J.; Jin, C.; Tian, J.; Strasser, P.; Yang, R.; MnCo_2O_4 Anchored on P-Doped Hierarchical Porous Carbon as an Electrocatalyst for High-Performance Rechargeable Li-O₂ Batteries. *ACS Catal.* **2015**, *5*, 4890-4896.

- (39) Liu, S.; San Hui, K.; Hui, K. N.; Yun, J. M.; Kim, K. H.; Vertically stacked bilayer $\text{CuCo}_2\text{O}_4/\text{MnCo}_2\text{O}_4$ heterostructures on functionalized graphite paper for high-performance electrochemical capacitors. *J. Mater. Chem. A* **2016**, *4*, 8061-8071.
- (40) Wang, S.; Hou, Y.; Wang, X. Development of a Stable MnCo_2O_4 Cocatalyst for Photocatalytic CO_2 Reduction with Visible Light. *ACS Appl. Mater. Interfaces* **2015**, *7*, 4327-4335.
- (41) Qiu, M.; Zhan, S.; Yu, H.; Zhu, D.; Wang, S. Facile preparation of ordered mesoporous MnCo_2O_4 for low-temperature selective catalytic reduction of NO with NH_3 . *Nanoscale* **2015**, *7*, 2568-2577.
- (42) Ma, C. Y.; Mu, Z.; Li, J. J.; Jin, Y. G.; Cheng, J.; Lu, G. Q.; Hao, Z. P.; Qiao, S. Z. Mesoporous Co_3O_4 and $\text{Au/Co}_3\text{O}_4$ catalysts for low-temperature oxidation of trace ethylene. *J. Am. Chem. Soc.* **2010**, *132*, 2608-2613.
- (43) Ge, X.; Liu, Y.; Goh, F. T.; Hor, T. A.; Zong, Y.; Xiao, P.; Zhang, Z.; Lim, S. H.; Li, B.; Wang, X.; Liu, Z. Dual-phase spinel MnCo_2O_4 and spinel $\text{MnCo}_2\text{O}_4/\text{nanocarbon}$ hybrids for electrocatalytic oxygen reduction and evolution. *ACS Appl. Mater. Interfaces* **2014**, *6*, 12684-12691.
- (44) Sing, K.S; Reporting physisorption data for gas/solid systems with special reference to the determination of surface area and porosity. *Pure Appl. Chem.* **1985**, *57*, 603-619.
- (45) Ravikovitch, P. I.; Neimark, A. V. Characterization of nanoporous materials from adsorption and desorption isotherms. *Colloids Surf. A Physicochem. Eng. Asp.* **2001**, *187*, 11-21.
- (46) Ren, Y.; Ma, Z.; Morris, R.E.; Liu, Z.; Jiao, F.; Dai, S.; Bruce, P.G. A solid with a hierarchical tetramodal micro-meso-macro pore size distribution. *Nat. Commun.* **2013**, *4*, 2015.

- (47) Li, L.; Zhang, Y.; Shi, F.; Zhang, Y.; Zhang, J.; Gu, C.; Wang, X.; Tu, J. Spinel Manganese–Nickel–Cobalt Ternary Oxide Nanowire Array for High-Performance Electrochemical Capacitor Applications. *ACS Appl. Mater. Interfaces* **2014**, *6*, 18040-18047.
- (48) Kong, D.; Luo, J.; Wang, Y.; Ren, W.; Yu, T.; Luo, Y.; Yang, Y.; Cheng, C. Three-Dimensional $\text{Co}_3\text{O}_4@\text{MnO}_2$ Hierarchical Nanoneedle Arrays: Morphology Control and Electrochemical Energy Storage. *Adv. Funct. Mater.* **2014**, *24*, 3815-3826.
- (49) Wu, Z. S.; Ren, W.; Wang, D. W.; Li, F.; Liu, B.; Cheng, H. M. High-energy MnO_2 nanowire/graphene and graphene asymmetric electrochemical capacitors. *ACS Nano* **2010**, *4*, 5835-5842.
- (50) Cui, J.; Zhang, X.; Tong, L.; Luo, J.; Wang, Y.; Zhang, Y.; Xie, K.; Wu, Y. A facile synthesis of mesoporous $\text{Co}_3\text{O}_4/\text{CeO}_2$ hybrid nanowire arrays for high performance supercapacitors. *J. Mater. Chem. A* **2015**, *3*, 10425-10431.
- (51) Chen, H. C.; Jiang, J. J.; Zhao, Y. D.; Zhang, L.; Guo, D. Q.; Xia, D. D. One-pot synthesis of porous nickel cobalt sulphides: tuning the composition for superior pseudocapacitance. *J. Mater. Chem. A* **2015**, *3*, 428-437.
- (52) Mondal, A. K.; Su, D.; Chen, S.; Ung, A.; Kim, H. S.; Wang, G. Mesoporous MnCo_2O_4 with a Flake-Like Structure as Advanced Electrode Materials for Lithium-Ion Batteries and Supercapacitors. *Chem. Eur. J.* **2015**, *21*, 1526-1532.
- (53) Chen, H.; Jiang, J.; Zhang, L.; Wan, H.; Qi, T.; Xia, D. Highly conductive NiCo_2S_4 urchin-like nanostructures for high-rate pseudocapacitors. *Nanoscale* **2013**, *5*, 8879-8883.
- (54) Xiao, Y.; Liu, S.; Li, F.; Zhang, A.; Zhao, J.; Fang, S.; Jia, D. 3D Hierarchical Co_3O_4 twin-spheres with an urchin-like structure: large-scale synthesis, multistep-splitting growth, and electrochemical pseudocapacitors. *Adv. Funct. Mater.* **2012**, *22*, 4052-4059.

Table of Content image

